FULL PAPER

# The Role of Hierarchical Morphologies in the Superior Gas Sensing Performance of CuO-Based Chemiresistors

*Diogo P. Volanti, Anderson A. Felix,\* Marcelo O. Orlandi, George Whitfield, Dae-Jin Yang, Elson Longo, Harry L. Tuller,\* and José A. Varela*

**The development of gas sensors with innovative designs and advanced functional materials has attracted considerable scientific interest given their potential for addressing important technological challenges. This work presents new insight towards the development of high-performance p-type semiconductor gas sensors. Gas sensor test devices, based on copper (II) oxide (CuO) with innovative and unique designs (urchin-like, fiber-like, and nanorods), are prepared by a microwave-assisted synthesis method. The crystalline composition, surface area, porosity, and morphological characteristics are studied by X-ray powder diffraction, nitrogen adsorption isotherms, field-emission scanning electron microscopy and high-resolution transmission electron microscopy. Gas sensor measurements, performed simultaneously on multiple samples, show that morphology can have a substantial influence on gas sensor performance. An assembly of urchin-like structures is found to be most effective for hydrogen detection in the range of parts-per-million at 200 °C with 300-fold larger response than the previously best reported values for semiconducting CuO hydrogen gas sensors. These results show that morphology plays an important role in the gas sensing performance of CuO and can be effectively applied in the further development of gas sensors based on p-type semiconductors.**

## 1. Introduction

Morphology-dependent physical and chemical properties of micro-,[1] meso-,[2] and nanomaterials,[3] with stable and controlled size and shape, have been widely studied with the objective of enhancing the performance of metal oxide semiconducting gas sensors.[4–7] Different materials and sensor designs are employed as means of improving sensor selectivity, sensitivity, response time, and for decreasing the working temperature in both p- and n-type semiconductor gas sensors.[8–13] Approaches in n-type materials have included control of, for example, the character of exposed crystallographic planes, grain and pore morphology, and surface functionalization with catalytic metals.[6–14] Sensors based on hierarchically porous structures or hollow microsphere templates provide higher surface-to-volume ratios, with reduced tendency to form agglomerates due to their larger dimensions.[6,14–18] This allows for fast and effective gas adsorption onto the entire sensing surface simultaneously, improving sensitivity and response time.[17,19] While a great deal of attention has been focused on n-type semiconducting oxides, few studies have been focused on the factors that influence and control the behavior of p-type gas sensors. Among p-type oxide semiconductors, copper (II) oxide (CuO) has been investigated for a wide range of applications including catalysis, fuel cells, and solar cells, among others.[20–27] Single-phase CuO, or CuO as part of heterojunction sensors, has demonstrated considerable potential for the detection of gases, such as $C_2H_5OH$, $H_2S$, $H_2$, CO, $NH_3$ and HCN.[28–34] However, experimental results obtained with CuO-based sensors, to date, are difficult to compare, given the different experimental and gas sensing procedures used in these studies.

In the present study, a series of CuO nanostructured materials, with different and controlled morphologies, are simultaneously examined within the same test apparatus, enabling a more systematic assessment of sensor response, crucial for understanding the influence of morphology on gas sensing performance. Gas sensor test devices were assembled using single-phase CuO nanostructured materials prepared by microwave-assisted synthesis (MWA) method with different morphologies, including hierarchical urchin-, fiber- and nanorod structures.

Dr. D. P. Volanti, Dr. A. A. Felix, Prof. M. O. Orlandi,
Prof. E. Longo, Prof. J. A. Varela
Departamento de Físico-Química
Instituto de Química
Universidade Estadual Paulista (UNESP)
Araraquara, SP, 14800-900, Brazil
E-mail: aafelixy@yahoo.com.br
Dr. A. A. Felix, Dr. G. Whitfield, Dr. D.-J. Yang,[+] Prof. H. L. Tuller
Department of Materials Science and Engineering
Massachusetts Institute of Technology (MIT)
Cambridge, MA, 02139, USA
E-mail: tuller@mit.edu
[+] Present address: Materials Research Laboratory, Samsung Advanced
Institute of Technology, Samsung Electronics Corporation, Yongin-Si,
Gyeonggi-Do 446-712, Republic of Korea

## 2. Results and Discussion

CuO samples were prepared by the MWA growth method with different morphologies, achieved by use of different bases

ADVANCED
FUNCTIONAL
MATERIALS
www.afm-journal.de

*Materials Views*
www.MaterialsViews.com
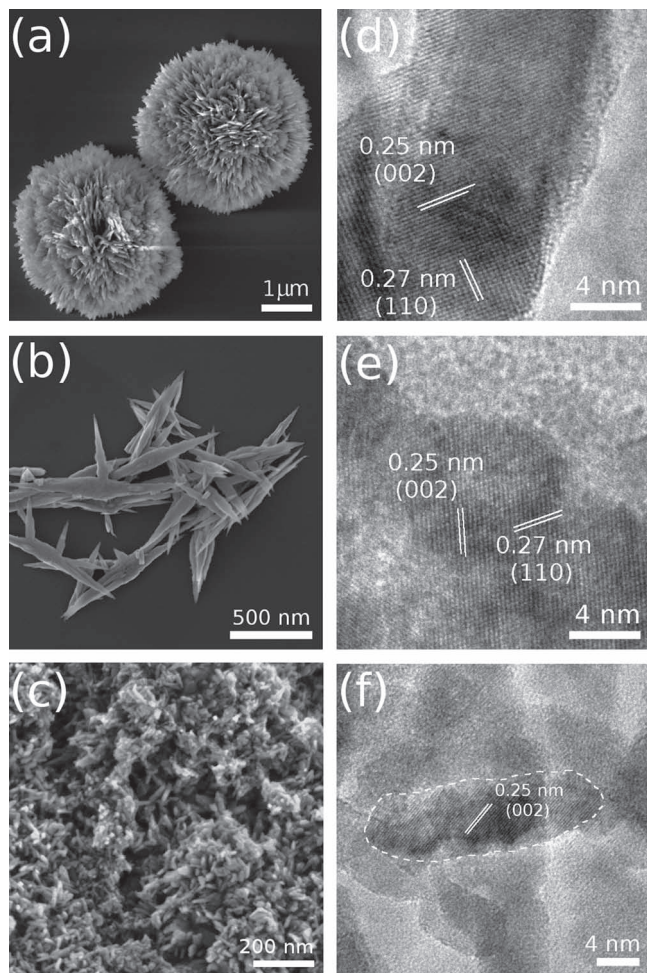
**Figure 1.** FESEM images of as-prepared CuO-based gas sensor materials with a) urchin-like, b) fiber-like, and c) nanorods shaped following the MWA synthesis procedure. HRTEM images of d) single urchin spine, e) the edge region of a fiber, and f) a single nanorod.

and solvents as described in detail in our previous work.[24] **Figure 1**a shows an field emission scanning electron microscopy (FESEM) image of CuO with an urchin-like morphology. These structures are ≈3 μm in diameter and are composed of a polycrystalline solid center with nanostructured spines with length of approximately 100 nm and width of 10 nm.[35] CuO fiber-like structures with length of ≈1 μm and width of up to 150 nm (Figure 1b) and CuO nanorods ≈30 nm long (Figure 1c) are also shown. Recent work demonstrated that the gas-sensing properties of n-type sensors could be improved by exposing their high-energy surface crystallographic planes and so this feature was investigated as well in this study.[36–39] High-resolution transmission electron microscopy (HRTEM) was used to characterize the detailed distribution of crystal planes, as shown in Figure 1d–f. The HRTEM images show that the spines of the urchin-like structures and fibers are single crystals with triangular shape (Figure 1d,e) and with interplanar distances of 0.27 and 0.25 nm, related to the CuO tenorite (110) and (002) planes, respectively. Moreover, the fiber-like structures have characteristics typical of a mesocrystal, believed to be the consequence

of growth by oriented attachment, but without a well-faceted morphology. Furthermore, the nanorods are also crystalline and HRTEM image (Figure 1f) also presents the same interplanar distances as the other two samples. The CuO morphologies, after gas sensor tests, show that the morphologies remained invariant after sensor characterization (Figure S1, Supporting Information). This suggests that CuO nanostructured materials, prepared by MWA with post-annealing, should retain their respective morphologies even under sensor operating conditions.

All three specimens were identified by X-ray powder diffraction (XRD) as having the CuO tenorite monoclinic structure (JCPDS No. 48-1548 and space group C2/c) (**Figure 2**a). No peaks characteristic of secondary phases were observed. The different peak intensities and the relative broadening of specific peaks for each sample are compatible with the formation of crystals of different dimensions; i.e., lower intensities and enlarged peaks for nanorods as compared to micro-dimensioned materials (fiber- and urchin-like). These results show the high phase purity and crystallinity of the CuO prepared by MWA.

Gas sensor performance is very sensitive to the morphological parameters such as surface area and porosity.[40,41] In order to determine these parameters, nitrogen adsorption and
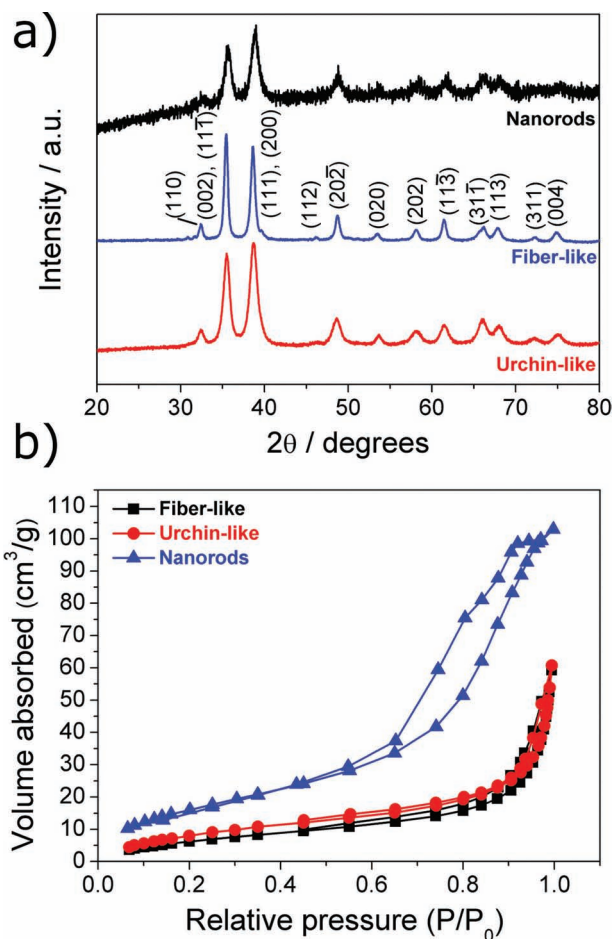


**Figure 2.** a) Powder XRD patterns and b) nitrogen adsorption–desorption isotherms for CuO-morphologies.

Materials
Views
www.MaterialsViews.com

ADVANCED
FUNCTIONAL
MATERIALS
www.afm-journal.de

desorption (BET) measurements were performed on the sensor materials (Figure 2b). The $N_2$ isotherms (related to the type III isotherm in the IUPAC classification) exhibit type H3 loops, indicating that all samples have a similar pore size distribution, i.e., average pore size of ≈2–50 nm in diameter.[42] The pore size distributions observed for urchin- and fiber-like samples are very similar and probably reflect sample porosity related to particle dimensions comparable with pore size. However, the nanorods have a larger pore size distribution than its dimensions, probably related to the aggregation of the CuO nanorods. On the other hand, the measured specific surface areas of the urchin-, fiber- and nanorod structures were 26 $m^2$ $g^{-1}$, 35 $m^2$ $g^{-1}$ and 64 $m^2$ $g^{-1}$, respectively. These results indicate that the urchin- and fiber-like structures have similar surface areas, while nanorods have roughly double the surface area.

Semiconductor gas sensor response is highly influenced by parameters such as operating temperature and gas concentration.[43] Thus, the comparison of gas sensor response for the same material with different morphologies can best be accomplished if the response of the ensemble of sensors can be measured simultaneously, under identical experimental conditions. In order to enable such an in situ comparison, a gas-sensor system enabling the measurement of up to eight gas sensors test devices simultaneously, co-situated in the same chamber, was developed (see gas sensor system in the Experimental Section). The gas sensor test devices were prepared by depositing drops of solutions of the three different CuO particle morphologies onto alumina substrates with interdigitated gold electrodes (Figure S2, Supporting Information) and were tested as function of the operating temperature and gas concentration of respective oxidizing and reducing gases.

**Figure 3** and **4** show the sensor signal and response time of the different CuO morphologies as functions of the operating temperature and gas concentration. The sensor signal or response ($R_{gas}/R_{air}$ or $R_{air}/R_{N_2}$) is defined as the ratio of the sensor resistance measured when exposed to the target gas ($R_{gas}$) to the resistance in the air reference ($R_{air}$) for reducing

gases and vice versa for oxidizing gases, i.e., ($R_{air}/R_{gas}$). The response time is defined as the time needed to reach 90% of the final steady state signal.[43,44,45] It is known that when oxidizing molecules are adsorbed onto an n-type oxide surface, a depletion layer is formed in response, resulting in an increase of the sensor resistance. The reverse is expected for a p-type gas sensor, i.e., oxidizing gases will induce an accumulation of holes near the surface resulting in a decrease in resistance, while reducing gases, on the other hand, will deplete holes near the surface, resulting in an increase in resistance. Our results show that each of the CuO gas sensor test devices responded as expected for p-type semiconductors and were sensitive to both reducing ($H_2$ and CO) and oxidizing ($O_2$ and $NO_2$) gases. Furthermore, they displayed reversible sensor response down to the lowest exposure levels and temperatures (see Figure S3-S6 in Supporting Information). For all gases tested, above 200 °C, the sensor signals decreased with increasing temperature (Figure 4a–d) and increased with increasing gas concentration (Figure 3 and Supporting Information Figure S7) and the response time (insets in Figure 4b–d) is always shorter at higher temperatures (very slightly for CO and $NO_2$) and increases with decreasing temperature and decreases with increasing gas concentration (Figure S7, Supporting Information) for all samples.

**Figure 5** shows the selectivity of $H_2$ in relation to CO and $NO_2$ for 50 ppm levels of exposure for a series of operating temperatures for the three designated types of CuO gas sensors. In this work, the selectivity is defined as the ratio of the sensor signal generated when exposed to the test gas versus that obtained for potential cross sensitive gases, i.e., ($S_{H_2}/S_{CO}$) or ($S_{H_2}/S_{NO_2}$).[43] As evident from Figure 5, all of the CuO specimens exhibit selectivities to $H_2$ greater than unity when compared to CO or $NO_2$. The results show that the urchin-like structures exhibit the largest $H_2$ selectivity with values of two or greater for all gas concentrations at temperatures in the range of 200–250 °C (see insets). On the other hand, fiber-like and nanorod structures have selectivities less than 1.5 to $NO_2$ and CO, for nearly the full range of gas concentrations and temperatures. Overall, the urchin-like CuO particles showed the highest sensitivity, with rods somewhat more sensitive than fibers.

As expected and in accordance to the ionosorption model,[46,47] molecules of oxidizing gases are adsorbed onto a CuO surface and chemisorption proceeds by the transfer of electrons from the surface to the oxidizing gas molecules. This in turn results in a lowering of the Fermi level, leading to increased hole density near to the surface and, consequently, decreased resistance. The reverse occurs for reducing gases, i.e., by the transfer of electrons from the reducing gas molecules to the surface, leading to depletion of holes near the surface, resulting in an increase in resistance. In addition, the sensor signal and response time are sensitive to gas diffusion effects and the rate of surface reaction, the latter due to the different adsorption/desorption energies for the different adsorbed species at the sensor surface as functions of operating temperature and gas concentration.[48,49] A recent theoretical study, using $SnO_2$ as model, show that the oxygen ion species ($O_2^-$, $O^-$, $O^{2-}$) ionosorbed on the surface depends on the temperature of operation.[50] Based on this model and the measurements of conductance vs. inverse temperature (see inset Figure 4a), we expect that ionosorption of physisorbed oxygen (Reaction 1) on
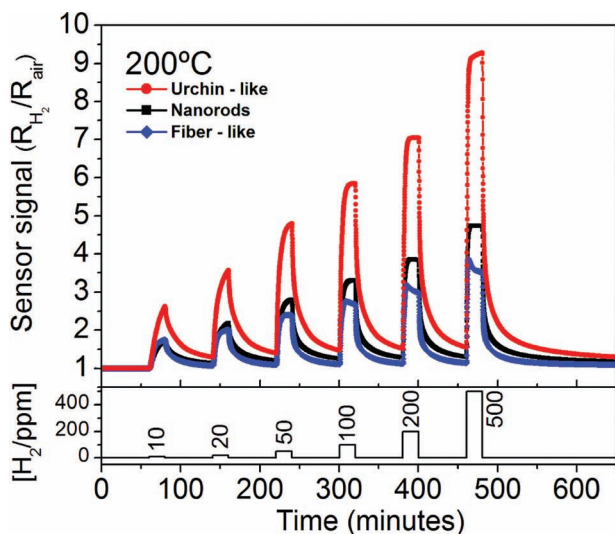


**Figure 3.** $H_2$ gas sensor response plots as function of the gas concentration at 200 °C for the CuO-morphologies.
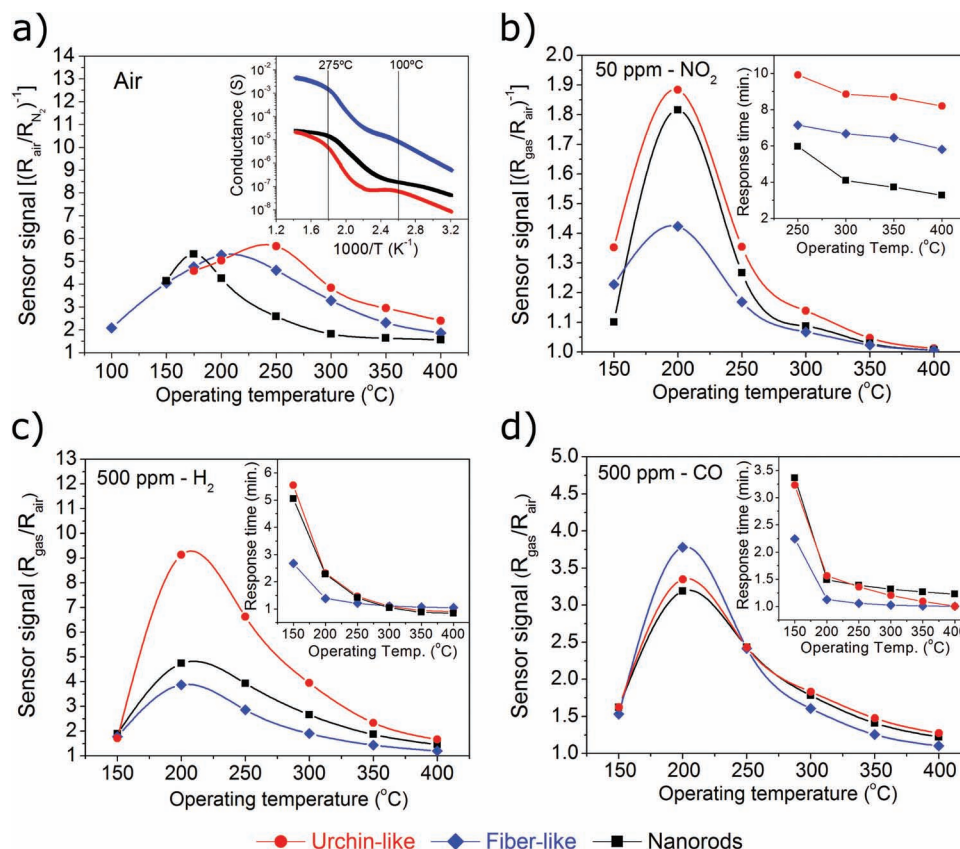
**Figure 4.** Gas response plots to a) air, b) 50 ppm $NO_2$, c) 500 ppm $H_2$, and d) 500 ppm CO, as a function of operating temperature for different CuO morphologies. The insets show a) conductance versus $1/T$ in air and b–d) the response time for each respective gas concentration as a function of operating temperature.

the CuO surface forming $O_2^-$ species (Reaction 2) occurs above 100 °C and only these species are chemisorbed up to 275 °C. Above this temperature, ionosorption of $O^-$ species (Reaction 3) begins with its concentration increasing with increasing temperature.

$$O_{2(gas)} \leftrightarrow O_{2(ads)} \tag{1}$$

$$O_{2(ads)} + e^- \leftrightarrow O_{2\ (ads)}^- \tag{2}$$

$$O_{2\ (ads)}^- + e^- \leftrightarrow O_{2\ (ads)}^{2-} \leftrightarrow 2O_{(ads)}^- \tag{3}$$

Reaction 3 is expected to be less effective in p-type materials given the low electron concentration, leading to a lower response to $O^-$ than $O_2^-$ oxygen species, consistent with results shown in Figure 4a. Similarly, one expects chemisorption of $NO_2$ to proceed as $NO_{2(gas)} + e^- \leftrightarrow NO_{2\ (ads)}^-$ from 150°C.[51] This mechanism, together with oxygen adsorption, contributes to the total surface charge density. However, sensitivity to $NO_x$ is reduced in p-type materials, given low electron concentrations and competition with oxygen species particularly at lower $NO_2$ partial pressures. At the same time, p-type materials are reportedly more selective and exhibit higher catalytic activity for reducing than for oxidizing gases. $H_2$ molecules interact with holes from the CuO surface, forming $H^+$ species above 150 °C

and then reacting with adsorbed oxygen to form hydroxyl groups according to the reactions:[52,53]

$$H_{2(gas)} + 2h^+ \leftrightarrow 2H_{(ads)}^+ \tag{4}$$

$$H_{(ads)}^+ + O_{2(ads)}^- \leftrightarrow OH_{(ads)} + \tfrac{1}{2}O_{2(gas)} \tag{5}$$

$$H_{(ads)}^+ + O_{(ads)}^- \leftrightarrow OH_{(ads)} \tag{6}$$
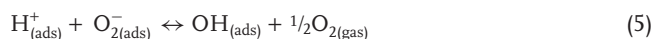
Similarly for adsorbed CO molecules, forming $CO^+$ species on CuO surfaces, described by:

$$CO_{(gas)} + h^+ \leftrightarrow CO_{(ads)}^+ \tag{7}$$

$$CO_{(ads)}^+ + O_{2(ads)}^- \leftrightarrow CO_{2(ads)} + \tfrac{1}{2}O_{2(gas)} \tag{8}$$

$$CO_{(ads)}^+ + O_{(ads)}^- \leftrightarrow CO_{2(ads)} \tag{9}$$

The adsorption of CO on CuO, however, leads to the formation of $Cu^+$–CO carbonyls, which can reduce the number of sensor active sites and block Reactions 8 and 9.[54] These results suggest that the enhanced response of $H_2$ versus CO and $NO_2$ depends on several factors including the larger number of

Makrials
Views
www.MaterialsViews.com

ADVANCED
FUNCTIONAL
MATERIALS
www.afm-journal.de

FULL PAPER
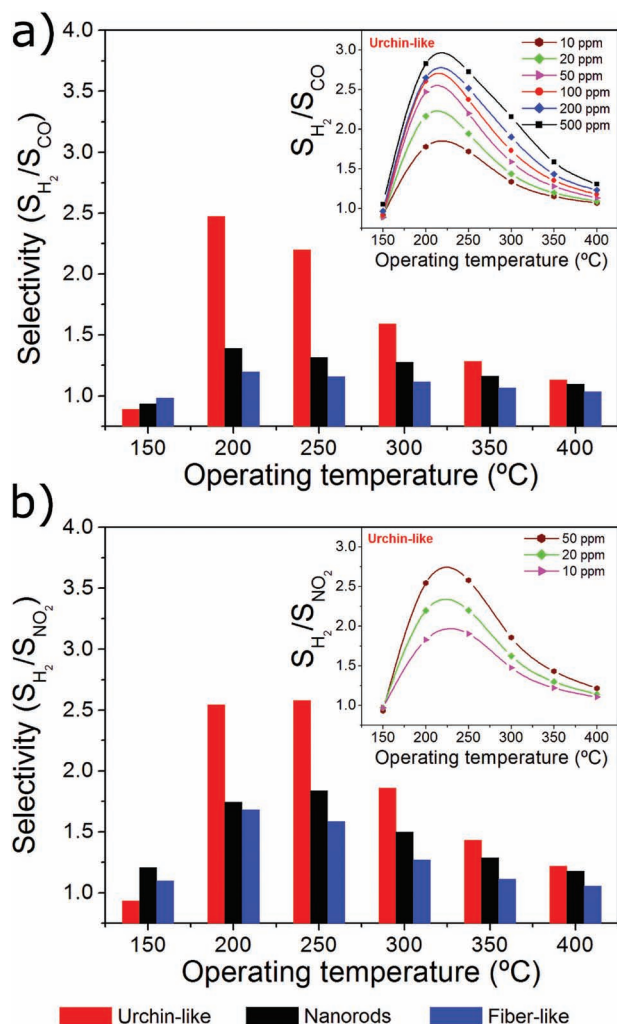
**Figure 5.** Selectivity of H$_2$ in relation to a) CO and b) NO$_2$ for 50 ppm levels of exposure gas as function of operating temperatures for the three designated types of CuO gas sensors. A standard value of 50 ppm was selected for the different gases to analyze for the effects of morphology, disregarding the different air quality standards for each test gases. The insets show the selectivity as function of operating temperatures and gas concentration for CuO urchin-like particles.



**Figure 6.** Shematic cartoon of particle-particle contacts and active sensing layer (left) and for comparison the FESEM overview images of CuO gas sensor test devices as-prepared (right) for a) urchin-like, b) fiber-like, and c) nanorods. The black and orange region on cartoon are correponding to bulk resistance and Debye-layer (sensing layer), respectively, and gray is electric contact.

holes induced per molecule and the adsorption/desorption surface mechanisms at low temperatures, which could be related, in part, to the blockage of active sites in the case of CO by carbonyls, formation of hydroxyl groups and competition between NO$_x$ and oxygen species.[55–57] Both of these effects could contribute to the observed incomplete recovery of the resistance to the baseline at reduced temperatures.

One further notes that the relative sensitivity and response time of the different CuO morphologies differ depending on the gas and temperature as can be observed in Figure 4. For example, the response to H$_2$ by the urchin-like structures is always superior; for exposure to NO$_2$, the difference between the different morphologies becomes smaller, while for CO, the fiber-like structures actually displays a somewhat higher sensitivity at low temperatures. These results point to the possible influence of morphology on the gas diffusion and surface

reaction effects resulting from the different assembly of the CuO structures (see **Figure 6**).[48,57]

While the gas-solid interactions can provide an explanation for the different response time and improvement of hydrogen selectivity for all CuO morphologies, they cannot, in themselves, explain the higher sensor signal exhibited by the urchin-like structures when compared to other morphologies. It is well known that gas sensor performance in nanoscale materials is highly sensitive to BET surface area when compared to materials with larger particle size.[58] This could explain the higher sensor signal of nanorods versus fiber-like structures; however, it cannot explain the superior response observed for the urchin-like structures over the two other structures. One could imagine that the nature of the exposed crystallographic planes could impact the selectivity of CuO gas sensors, given the different surface energies of various exposed planes.[59] In our study, however, urchin- and fiber-like structures have the same exposed crystallographic planes and still exhibit different sensor signals. This suggests that the nature of the exposed planes may

not be the main source of the enhanced sensor response of the CuO urchin-like structure. Certainly, area is not the source, since the urchin-like structures exhibited the smallest surface area of the three.

In a recent study, a model for the gas-sensing response and conduction in p-type materials was proposed, which focuses on the relationship between the active sensing layer (Debye-layer) resistance and the grain-to-grain contact resistance, both of which are gas sensitive.[60] This model suggests that the sensor resistance changes are related to the geometrical/morphological parameters of the samples and are proportional to the ratio of active sensing length (Debye-layer length) ($L_D$) to effective contact area ($D_C$) and to grain diameter ($D_G$), respectively, which can be expressed by

$$S = \frac{R_{gas}}{R_{air}}$$
$$= \frac{\frac{L_D}{D_C}\exp\left(-\frac{qV_{Air}}{2kT}\right)\exp\left(-\frac{\Delta\Phi}{2kT}\right) + \frac{1}{1+\frac{L_D}{D_G}\exp\left(-\frac{qV_{Air}}{2kT}\right)\exp\left(-\frac{\Delta\Phi}{2kT}\right)}}{\frac{L_D}{D_C}\exp\left(-\frac{qV_{Air}}{2kT}\right) + \frac{1}{1+\frac{L_D}{D_G}\exp\left(-\frac{qV_{Air}}{2kT}\right)}} \quad (10)$$

where $qV_{Air}$ is the surface potential barrier in air reference, $\Delta\Phi$ is the difference in the surface potential barrier when exposed to the gas of interest versus the value in air, $T$ is absolute temperature and $k$ is the Boltzmann constant. This equation suggests that the sensor signal can be improved by changing the shape and/or dimensions of grains and sensing layers, with the highest changes in sensor signal coming from the effective contact area reduction. In light of these predictions, the superior performance exhibited by the urchin-like structures may be a consequence of the nature of the particle-particle contacts and large particle size. This unique morphology can be seen to enhance the importance of particle-particle contacts, due to the lower effective contact area ($D_C$) and the multiple particle to particle contacts between the many spines, and the larger particle size ($D_G$), which can improve both terms in Equation 10.[60] In a similar way, the lower effective contact area of the nanorods versus that of the fiber-like structure could contribute to the enhanced gas sensor response of the first morphology. Figure 6 shows overview SEM images of the samples as-prepared for gas sensor testing and schematic cartoons of particle-particle contacts and particle size for the different morphologies (preserving the respective dimensions of the samples). Before one can affirm whether indeed the particle-particle contact in CuO samples is the performance determining factor rather than the change in resistance of the individual particles or the electrode/semiconductor interface, additional studies must be made to deconvolute the various contributions to the overall sensor resistance. Impedance studies on well-defined model structures have been initiated which we expect will be able to address these questions more directly. Otherwise, this model does provide a working phenomenological explanation for the improvement of sensor signal exhibited by the urchin-like structures, which together with the advantageous hydrogen surface reactions discussed above, can explain the higher hydrogen selectivity of this specific morphology.

In summary, the urchin-like CuO morphology was found to exhibit the best performance of the three types of CuO particles studied, showing higher hydrogen sensitivity combined with

relatively low operating temperature (200 °C), particularly when compared to other semiconducting oxides such as $SnO_2$, commonly studied for $H_2$ detection.[10,48] The maximum sensor signal at 500 ppm of $H_2$ (9.3) at 200 °C is more than 300-fold larger than the best reported values for CuO-single phase gas sensors.[30,61] The sensor signal was found to follows a power law dependence on gas concentration of the form $R \propto p_{H_2}^\beta$, with $\beta$ in this case taking on the value of 0.30.[9,43] Assuming that this dependence continues to hold to higher $H_2$ concentrations, a sensor response of ≈35 is estimated for an exposure to 4% $H_2$ (the lower flammable limit (LFL) of hydrogen in air)[62] pointing to the CuO urchin-like structure as a promising candidate for gas safety applications. An exceptionally low lower detection limit (LDL) around 300 ppb was estimated for the CuO urchin-like structures (see Figure S8 in the Supporting Information), which is comparable to that observed for $SnO_2$-based gas sensors.[10] Thus, to the best of our knowledge, our results represent, by far, the highest hydrogen sensitivity exhibited by p-type chemiresistor sensors and better than many n-type -based gas sensors.[63] Furthermore, these high sensitivity CuO-based sensor devices can be prepared at considerably low cost and simplified manufacture when compared to other comparable test devices exhibiting superior hydrogen detection.[64]

## 3. Conclusions

In summary, a systematic examination of the sensor performance of a series of CuO-based nanostructured test devices with different morphologies (urchin-like, fiber-like and nanorods) exposed to reducing and oxidizing gases over a range of temperatures and gas concentrations were measured simultaneously in the same test chamber. These morphologies present good thermal and chemical stability in air with the higher hydrogen sensor signal exhibited by the urchin-like morphology. The hydrogen sensitivity observed for this morphology is more than 300-fold larger than the best reported for CuO-single phase gas sensors. Explanations for this behavior were proposed, identifying large particle size and particle-to-particle contacts as likely sources of the improved performance. These results point to morphology control as being an effective tool in improving the performance in single-phase p-type gas sensors.

## 4. Experimental Section

*Morphology, Structure, Surface Area and CuO Porosity Characterization*: The morphology, diameter, width and length of the nanostructures were initially investigated using a JEOL, model JSM-7500F electron microscope operated at an accelerating voltage of 2 kV. Samples were first dispersed in isopropyl alcohol, then sonicated for 5 min and finally deposited onto Si wafers, which were ultimately attached onto the surfaces of FESEM brass stubs, using conductive carbon tape. Specimens for HRTEM were obtained by dripping droplets of as-prepared samples from an ethanol dispersion, which had been sonicated for 5 min, onto 300 mesh Cu grids, followed by drying. HRTEM images were then taken at an accelerating voltage of 200 kV on a Philips model CM200 instrument. Crystallographic information for as-synthesized samples was collected by a Rigaku DMax 2500PC X-ray diffractometer, operated at 40 kV, 150 mA using Cu K$\alpha$ ($\alpha$ = 1.5406 Å) radiation. Data were collected in the $2\theta$ range between 20° and

www.MaterialsViews.com

ADVANCED
FUNCTIONAL
MATERIALS
www.afm-journal.de

FULL PAPER

80° with a 0.5° divergence slit, a 0.3 mm receiving slit and in a fixed-time mode with 0.02° step size. The specific surface area of the resulting materials was determined by the Brunauer–Emmett–Teller (BET) method measured at 77 K on an ASAP2010 apparatus (Micromeritics, Norcross, GA, USA) and the pore size distribution was calculated by the Barret–Joyner–Halenda (BJH) method under 77 K nitrogen desorption.

*Gas Sensor Preparation*: The CuO powders were dispersed in isopropyl alcohol using an ultrasonic cleaner and then the suspension was dripped directly onto alumina substrates with interdigitated gold electrode arrays (200 μm Au fingers spaced 200 μm apart). The substrates were then heated to 100 °C for 15 min to evaporate the solvent, followed by calcination at 500 °C for 2 h, to stabilize the sample before the gas sensing measurements were performed.

*Gas Sensor System and Measurements*: LabVIEW software was written to control simultaneously and remotely the gas flow, temperature and sample resistance monitoring of up to eight gas sensor test devices in the same chamber. Gas sensing tests were carried out by monitoring changes of resistance in all eight channels (using Data acquisition switch unit HP34970A with input impedance of $1.2 \times 10^{+8}$ Ω and delay of 4 s by point) during cyclic exposure to different concentrations of testing gas. For the oxygen test, clean dry air was used as the oxygen source with dry $N_2$ as balance gas. For $H_2$ and CO (between 10 to 500 ppm) and $NO_2$ (between 1 to 50 ppm) test gases were diluted in dry air with dry air as balance gas. To achieve this, certified pre-mixed gas mixtures, containing a trace of the test gases diluted in dry air ($H_2$ and CO (1000 ppm) and $NO_2$ (100 ppm)) (BOC GASES) were mixed with clean dry air, using mass flow controllers (MKS). The total gas flow rate (test gas plus balance gas) was kept constant (200 sccm) during these tests. The sensor test devices were equilibrated in dry air for 12 h at each temperature before the beginning of each gas sensor measurement to insure a stable and reproducible baseline resistance. Pt/Pt-Rh (type S) thermocouples were used to measure temperature in situ and gas sensor measurements were performed at 50 °C intervals in the range between 100 °C and 400 °C, with rate heating of 3 °C/min.

## Supporting Information

## Acknowledgements

[1] Z. Jing, J. Zhan, *Adv. Mater.* **2008**, *20*, 4547–4551.
[2] H. Nguyen, S. A. El-Safty, *J. Phys. Chem. C* **2011**, *115*, 8466–8474.
[3] O. S. Kwon, J. Y. Hong, S. J. Park, Y. Jang, J. Jang, *J. Phys. Chem. C* **2010**, *114*, 18874–18879.
[4] G. Jimenez-Cadena, J. Riu, F. X. Rius, *Analyst* **2007**, *132*, 1083–1099.
[5] Z. P. Li, Q. Q. Zhao, W. L. Fan, J. H. Zhan, *Nanoscale* **2011**, *3*, 1646–1652.
[6] A. Gurlo, *Nanoscale* **2011**, *3*, 154–165.
[7] D. Barreca, E. Comini, A. P. Ferrucci, A. Gasparotto, C. Maccato, C. Maragno, G. Sberveglieri, E. Tondello, *Chem. Mater.* **2007**, *19*, 5642–5649.
[8] D. D. Li, J. Hu, R. Q. Wu, J. G. Lu, *Nanotechnology* **2010**, *21*, 485502–485502.
[9] I.-D. Kim, A. Rothschild, B. H. Lee, D. Y. Kim, S. M. Jo, H. L. Tuller, *Nano Lett.* **2006**, *6*, 2009–2013.
[10] D.-J. Yang, I. Kamienchick, D. Y. Youn, A. Rothschild, I.-D. Kim, *Adv. Funct. Mater.* **2010**, *20*, 4258–4264.
[11] I. D. Kim, A. Rothschild, T. Hyodo, H. L. Tuller, *Nano Lett.* **2006**, *6*, 193–198.
[12] Y.-E. Chang, D.-Y. Youn, G. Ankonina, D.-J. Yang, H.-G. Kim, A. Rothschild, I.-D. Kim, *Chem. Commun.* **2009**, 4019–4021.
[13] H.-R. Kim, A. Haensch, I.-D. Kim, N. Barsan, U. Weimar, J.-H. Lee, *Adv. Funct. Mater.* **2011**, *21*, 4402–4402.
[14] A. Gurlo, *Small* **2010**, *6*, 2077–2079.
[15] X. Wang, W. Liu, J. Liu, F. Wang, J. Kong, S. Qiu, C. He, L. Luan, *ACS Appl. Mater. Interfaces* **2012**, *4*, 817–825.
[16] G. Zhu, Y. Liu, H. Xu, Y. Chen, X. Shen, Z. Xu, *CrystEngComm* **2012**, *14*, 719–725.
[17] G. Zhu, H. Xu, Y. Xiao, Y. Liu, A. Yuan, X. Shen, *ACS Appl. Mater. Interfaces* **2012**, *4*, 744–751.
[18] H. Zhang, Q. Zhu, Y. Zhang, Y. Wang, L. Zhao, B. Yu, *Adv. Funct. Mater.* **2007**, *17*, 2766–2771.
[19] Y. Zeng, T. Zhang, L. Wang, R. Wang, W. Fu, H. Yang, *J. Phys. Chem. C* **2009**, *113*, 3442–3448.
[20] X. P. Gao, J. L. Bao, G. L. Pan, H. Y. Zhu, P. X. Huang, F. Wu, D. Y. Song, *J. Phys. Chem. B* **2004**, *108*, 5547–5551.
[21] J. C. Park, J. Kim, H. Kwon, H. Song, *Adv. Mater.* **2009**, *21*, 803–807.
[22] S. Anandan, X. G. Wen, S. H. Yang, *Mater. Chem. Phys.* **2005**, *93*, 35–40.
[23] Y. Liu, L. Liao, J. Li, C. Pan, *J. Phys. Chem. C* **2007**, *111*, 5050–5056.
[24] D. P. Volanti, A. G. Sato, M. O. Orlandi, J. M. C. Bueno, E. Longo, J. Andrés, *ChemCatChem* **2011**, *3*, 839–843.
[25] C. L. Chang, C. C. Hsu, T. J. Huang, *J. Solid State Electrochem.* **2003**, *7*, 125–128.
[26] D. Gamarra, A. Martinez-Arias, *J. Catal.* **2009**, *263*, 189–195.
[27] A. Hornes, P. Bera, A. L. Camara, D. Gamarra, G. Munuera, A. Martinez-Arias, *J. Catal.* **2009**, *268*, 367–375.
[28] J. Y. Li, S. L. Xiong, B. J. Xi, X. G. Li, Y. T. Qian, *Cryst. Growth Des.* **2009**, *9*, 4108–4115.
[29] N. S. Ramgir, S. K. Ganapathi, M. Kaur, N. Datta, K. P. Muthe, D. K. Aswal, S. K. Gupta, J. V. Yakhmi, *Sens. Actuators B* **2010**, *151*, 90–96.
[30] N. D. Hoa, S. Y. An, N. Q. Dung, N. Van Quy, D. Kim, *Sens. Actuators, B* **2010**, *146*, 239–244.
[31] R. K. Bedi, I. Singh, *ACS Appl. Mater. Interfaces* **2010**, *2*, 1361–1368.
[32] M. Parmar, R. Bhatia, V. Prasad, K. Rajanna, *Sens. Actuators, B* **2011**, *158*, 229–234.
[33] M. Yang, J. He, X. Hu, C. Yan, Z. Cheng, *Environ. Sci. Technol.* **2011**, *45*, 6088–6094.
[34] M. Yang, J. He, X. Hu, C. Yan, Z. Cheng, Y. Zhao, G. Zuo, *Sens. Actuators, B* **2011**, *155*, 692–698.
[35] D. P. Volanti, M. O. Orlandi, J. Andrés, E. Longo, *CrystEngComm* **2010**, *12*, 1696–1699.
[36] X. Han, M. Jin, S. Xie, Q. Kuang, Z. Jiang, Y. Jiang, Z. Xie, L. Zheng, *Angew. Chem. Int. Ed.* **2009**, *48*, 9180–9183.
[37] H. B. Jiang, Q. Cuan, C. Z. Wen, J. Xing, D. Wu, X.-Q. Gong, C. Li, H. G. Yang, *Angew. Chem. Int. Ed.* **2011**, *50*, 3764–3768.
[38] X.-G. Han, H.-Z. He, Q. Kuang, X. Zhou, X.-H. Zhang, T. Xu, Z.-X. Xie, L.-S. Zheng, *J. Phys. Chem. C* **2008**, *113*, 584–589.
[39] X. Wang, X. Han, S. Xie, Q. Kuang, Y. Jiang, S. Zhang, X. Mu, G. Chen, Z. Xie, L. Zheng, *Chem. Eur. J.* **2012**, *18*, 2283–2289.
[40] K. Sahner, H. Tuller, *J. Electroceram.* **2010**, *24*, 177–199.
[41] N. Barsan, U. Weimar, *J. Electroceram.* **2001**, *7*, 143–167.

**FULL PAPER**

[42] S. J. Gregg, K. S. W. Sing, *Adsorption, surface area, and porosity*, Academic Press, London **1991**.

[43] J. L. G. Fierro, *Metal Oxide Chemistry and Applications*, CRC Press, Boca Raton **2006**.

[44] M E. Franke, T J. Koplin, U. Simon, *Small* **2006**, *2*, 36–50.

[45] R. Waser, *Nanoelectronics and Information Technology: Advanced Electronic Materials and Novel Devices*, Wiley-VCH, Weinheim, Germany **2005**.

[46] M. J. Madou, S. R. Morrison, *Chemical Sensing with Solid State Devices*, Academic Press, New York **1989**.

[47] S. R. Morrison, *The Chemical Physics of Surfaces*, 2nd ed., Plenum Press, New York **1990**.

[48] G. Sakai, N. Matsunaga, K. Shimanoe, N. Yamazoe, *Sens. Actuators, B* **2001**, *80*, 125–131.

[49] D. E. Williams, G. S. Henshaw, K. F. E. Pratt, R. Peat, *J. Chem. Soc., Faraday Trans.* **1995**, *91*, 4299–4307.

[50] U. Pulkkinen, T. T. Rantala, T. S. Rantala, V. Lantto, *J. Mol. Catal. A: Chem.* **2001**, *166*, 15–21.

[51] B. J. Hansen, N. Kouklin, G. Lu, I. K. Lin, J. Chen, X. Zhang, *J. Phys. Chem. C* **2010**, *114*, 2440–2447.

[52] S. R. Morrison, *Sens. Actuators* **1987**, *12*, 425–440.

[53] A. Gurlo, R. Riedel, *Angew. Chem. Int. Ed.* **2007**, *46*, 3826–3848.

[54] K. I. Hadjiivanov, G. N. Vayssilov, *Advances in Catalysis* **2002**, *47*, 307–511.

[55] W. C. Conner, J. L. Falconer, *Chem. Rev.* **1995**, *95*, 759–788.

[56] T. Kida, T. Kuroiwa, M. Yuasa, K. Shimanoe, N. Yamazoe, *Sens. Actuators, B* **2008**, *134*, 928–933.

[57] S. Ahlers, G. Müller, T. Doll, *Sens. Actuators B* **2005**, *107*, 587–599.

[58] A. Rothschild, Y. Komem, *J. Appl. Phys.* **2004**, *95*, 6374–6380.

[59] J. Hu, D. Li, J. G. Lu, R. Wu, *J. Phys. Chem. C* **2010**, *114*, 17120–17126.

[60] N. Barsan, C. Simion, T. Heine, S. Pokhrel, U. Weimar, *J. Electroceram.* **2010**, *25*, 11–19.

[61] Improvement related to the ratio sensor signal ($S$) and gas concentration ($\rho$).

[62] T. Hübert, L. Boon-Brett, G. Black, U. Banach, *Sens. Actuators, B* **2011**, *157*, 329–352.

[63] N. G. Cho, G. C. Whitfield, D. J. Yang, H.-G. Kim, H. L. Tuller, I.-D. Kim, *J. Electrochem. Soc.* **2010**, *157*, J435–J439.

[64] J. Lee, D. H. Kim, S.-H. Hong, J. Y. Jho, *Sens. Actuators, B* **2011**, *160*, 1494–1498.